Fracture imaging using DAS-recorded microseismic events

Frantisek Stanek email: FStanek@mines.edu ORCID: 0000-0002-0037-9239

Ge Jin email: gjin@mines.edu ORCID: 0000-0002-9640-7547

Jim Simmons email: jsimmons@mines.edu ORCID: 0000-0000-0000-0000

Colorado School of Mines, Department of Geophysics, Golden, Colorado._

Key points:

1. Mapping fractures and understanding the reservoir response are the main goals of microseismic monitoring during hydraulic fracturing.

2. Distributed Acoustic Sensing provides high spatial resolution of microseismic reflections data.

3. The proposed fracture imaging workflow uses reflected shear waves in the time-space domain to map induced fractures in space domain.

Plain Language Summary:

Hydraulic fracturing is a stimulation technique enabling hydrocarbon production from unconventional reservoirs. The high-pressure injection creates fractures and increases permeability in the reservoir. Small earthquakes (microseismic events) are induced around newly created fractures in the stimulated area. By using fiber-optic-based Distributed Acoustic Sensing technology, we can record seismic waveforms generated by the microseismic events with very high spatial resolution. We observed seismic energy scattered at the created hydraulic fractures and used the energy to image the hydraulic fractures' geometry. The newly developed methodology can be used for mapping induced hydraulic fractures. Knowledge of fractures, their geometry and position, is important for understanding the reservoir response to injection and potentially increasing the effectiveness of the following operations.

Keywords:

AGU-index-terms:

0935 Seismic methods (3025, 7294) – Primary Index Term

8010 Fractures and faults – 1st term

7230 Seismicity and tectonics (1207, 1217, 1240, 1242) – 2nd term

0910 Data processing – 3rd term

0915 Downhole methods – 4th term

My keywords (up to six):

hydraulic fracturing, microseismic, DAS, Imaging, Reflection, fractures

ABSTRACT

Hydraulic fracturing enables hydrocarbon production from unconventional reservoirs. Mapping induced seismicity around newly created fractures is crucial for understanding the reservoir response and increasing the efficiency of operations. Distributed acoustic sensing (DAS) provides a large amount of high spatial resolution microseismic data acquired along the entire length of horizontal wells. We focus on the observed reflected S-waves and develop a new methodology to image induced fractures acting as reflectors in the media surrounding the events and monitoring fiber. The workflow consists of DAS data preprocessing, event location, wavefield separation, raytracing-based imaging, and image postprocessing. The comparison of the resulting fracture images with low-frequency DAS signals with fracture hits corroborates that the reflections are from fractures created by stimulation. The fracture imaging algorithm can be used for real-time mapping of fractures and tracking fracture changes in time. It leads to a better understanding of the reservoir response to hydraulic fracturing stimulation.

1. INTRODUCTION

Microseismic monitoring of hydraulic fracturing has been employed to understand the reservoir response and increase the efficiency of subsurface operations (Grechka and Heigl, 2017). Similarly, induced seismicity monitoring has been used during waste-water injection (e.g., Zoback, 2012), mining (e.g., Mendecki et al., 2010), enhancing of geothermal systems (e.g., Kwiatek et al., 2014), storing gas underground (e.g., Carannante et al., 2020) and CO_2 sequestration (e.g., Williams-Stroud et al., 2020) to mitigate seismic hazard.

A commonly provided result of hydraulic fracturing microseismic monitoring is a catalogue of detected microseismic events with their origin time, location of hypocenter, magnitude and, if possible, a description of source mechanism. The main, and challenging, goal is to describe fracture geometry and orientation, connectivity between individual fractures, and estimate the area of the rock volume having increased permeability. The interpretation is mostly done with Discrete Fracture Network (Williams-Stroud et al., 2013), Stimulated Rock Volume (Zeynal et al., 2014) and geomechanical models (e.g., Stanek et al., 2017). However, due to uncertainties in event locations and inverted fault planes, and lack of understanding what microseismicity really represents, more accurate knowledge of induced fracture systems is still in need.

Another technique to map induced fractures, instead of connecting located events, is reflection imaging using microseismic events as sources. Grechka et al. (2017), Reshetnikov et al. (2010) or Lin & Zhang (2016) observed reflected waves in data acquired by 3C geophone arrays and used them for microseismic imaging. Such imaging is not common probably because it is difficult to see reflected waves in the microseismic data acquired by sparse geophone arrays.

Recently, distributed fiber optic sensing technology (Hartog, 2017) providing dense monitoring data started to be employed in oil and gas industry as an alternative to the traditional seismic arrays. Fiber-optic-based monitoring is a quickly developing technology that has been used for measuring vibrations, tem-

perature, and strain for many different purposes (e.g., Baldwin, 2015). Specifically, Distributed Acoustic Sensing (DAS) is being utilized for a long-term monitoring of vibrations. The fiber working as a sensor can be installed along the whole length of the stimulated well (in-well monitoring) or offset wells (cross-well monitoring). The best practice seems to be cementing fiber behind casing for permanent monitoring, although it can also be installed temporarily. Such monitoring geometry allows detection of a high number of weak (i.e., low magnitude) microseismic events due to proximity to the stimulated area. DAS offers other advantages compared to borehole geophone arrays, such as broadband response (from mHz to tens of kHz), long aperture (several km long fiber) and dense spatial sampling (channel spacing can be < 1 m). The main downside of fiber-optic-based monitoring is a single-component axial strain measurement only in the direction along the fiber (Baird et al., 2019). This causes critical problems when locating and inverting source mechanism of microseismic event detected by a single fiber. However, there are ways to overcome this issue using multi-component, so called, helical optical fibers (Lim Chen Ning & Sava, 2018), monitoring carried out by deviated or L-shaped array (Verdon et al., 2020), or monitoring with two or more nearby fiber well(s) (e.g., Cole et al., 2018).

DAS provides high spatial resolution recordings enabling detailed analyses of wavefield and development of new processing methods leading to improved interpretations and better insight into the reservoir response. In passive seismic, we rely on induced microseismic events around the monitoring wells at a reasonable distance to detect them. Recorded waves (i.e., arrival times and amplitudes) contain information about event location relative to a monitoring array, radiation pattern due to source processes, and about the media between source and fiber. It includes also the structural features represented by reflected/refracted/diffracted waves arriving later after the direct body waves arrival (Lellouch & Biondi, 2021). In some DAS-based microseismic data, one may observe not only far-field but also near-field signal (Luo, Jin, & Stanek, 2021) which can be used for more precise source description, and dispersive guided waves providing properties of anomalous velocity layers and helping identification of events located inside or outside reservoir layer (Luo, Lellouch et al., 2021). While all the phenomena are recorded with high resolution, we can not only map fracture propagation based on microseismic events located along fractures but also image fractures making use of reflected waves.

Another type of fiber-optic-based measurements during hydraulic fracturing used to describe fractures is low-frequency (< 1 Hz) DAS (LFDAS). LFDAS measures strain changes (i.e., works as hybrid distributed strain sensing, DSS) induced by hydraulic fractures (Jin & Roy, 2017; Jin et al., 2021; Zhu & Jin, 2021). The detected strain signals represent fractures which were initiated at the offset well and reached the monitoring fiber well, so called fracture hits or frac-hits. Therefore, frac-hits are clear proof that the fractures have half-length longer than spacing between treatment and monitoring well. LFDAS data also shows time intervals when the fracture is opening (extension at the fracture and compression around) and when it is closing (extension around fracture) due to

the leak-off after injection.

In this study, we analyze selected examples of field DAS-based microseismic data acquired during multi-well hydraulic fracturing, focused on observed reflected S-waves and propose a new method for imaging fractures in the vicinity of induced microseismic events. Imaged fractures are compared to LFDAS frac-hits to corroborate that the imaged waves are reflected from newly created hydraulic fractures.

2. DATA AND METHODOLOGY

2.1. DAS Data and Observations

We analyze data from the Chalk Bluff project in the Denver-Julesburg (DJ) Basin in Colorado, USA. Figure 1 shows a map of the study area with position of the pad of horizontal wells drilled in a N-S direction through the target unconventional reservoir formations Codell and Niobrara at depths around 7400 - 7700 ft (TVD). The reservoir was hydraulically fractured in hundreds of stages along lateral parts of all the horizontal wells. DAS microseismic and LFDAS monitoring of the studied area was carried out by two fibers permanently installed outside the casing of the red wells in Figure 1.

We have analyzed several strong microseismic events visible in the continuous DAS data. The waveforms of most of the events are relatively simple with symmetrical moveouts of direct P- and S-waves, where S-wave signals are usually higher amplitude than P-waves. Here, we focus on three example events which have more complex wavefields. DAS data and initial spatial locations (taken from catalogue of events located from surface array, provided by the data owner) of the selected events are shown in Figure 1 (yellow stars). Events A and C have both clear direct P- and S-waves (marked as P_D, S_D), event B has only an S-wave visible probably because of the lower magnitude. All three events have reflected S-waves (marked as S_R) but event C has a very complex wavefield following the S-wave arrival. We also notice secondary, similarly looking, weaker events coming after and before the main event in the data of the events A and B, respectively. These repeated events most probably occurred at the same location as the main events but at slightly different times.

The observed reflected waves could represent either a fault, fracture, or velocity interface, acting as a reflector in the medium around event location at the time when microseismic event occurred. However, in our case, we can exclude the possibility of reflections from near-horizontal interfaces (i.e., bedding planes) based on traveltime moveout. Reflection from a horizontal interface would be recorded by most of the channels along the fiber and be symmetric around the apex with a moveout similarly to the direct P- and S-waves. We interpret the reflected S-waves as reflections from approximately near-vertical faults, or near-vertical fractures perpendicular to the horizontal fiber. Furthermore, the reflectors in all three cases are most probably either very close to, or directly intersecting the fiber, as we see that the arrivals of reflected S-waves and direct

S-waves merge to the same channels where the reflectors likely intersect with the fiber well.

Figure 1: Upper left: A map of the horizontal wells (running N-S) and their relative positions. Wells with permanently installed fiber are shown in red. The diagonal NW-SE wells shown in gray are previously drilled production wells in the Niobrara. The yellow stars represent examples of strong microseismic events (A, B, C). The seismic coherency map in the background may indicate potential faults in the Niobrara formation. Upper right and bottom: Examples of three representative microseismic events with direct P-waves (P_D), direct S-waves (S_D), converted S- to P-waves (SP) and reflected S-waves (S_R) recorded by DAS array. The events A and B are accompanied by another weaker event with very similar moveout indicating similar location but slightly different origin time. Event C shows more complicated reflections after the direct S-wave.

2.2. Fracture reflection imaging - methodology

The reflected S-waves observed in the DAS data indicate the presence of reflectors in the area between the event locations and the recording fiber. From the moveouts, we may expect that the reflector orientation is near-vertical and perpendicular to horizontal well. Our first attempt to explain reflected S-waves (Stanek & Jin, 2021) was simple traveltime modeling. We were able to fit manually picked arrival times of P-, S- and reflected S-waves sufficiently well with synthetic traveltimes using a homogeneous isotropic velocity model (velocity taken from an available sonic log) with a vertical reflector perpendicular to the monitoring fiber well. However, such a method is not optimal as it requires testing of many different positions, orientations, and lengths of reflector until synthetics fit the arrival times.

Here, we propose an imaging technique converting DAS microseismic data in time to an image with reflector position in space. The raytracing-based method is similar to that used for DAS VSP processing (Schultz, 2019). The imaging procedure is incorporated into the seven-step workflow (also shown in Figure 2):

(1) Input cut-out 0.3 s long chunk of DAS data containing detected event (as shown in Figure 1) is pre-processed. We down-sample data from 10 kHz to 1 kHz sampling rate in order to minimize data size and then apply a band-pass filter to preserve the signal of interest between 10 and 300 Hz.

(2) We manually pick (P- and) S-wave arrivals and relocate the event using a standard grid-search location algorithm minimizing the L1-misfit. This way we improve the origin time and initial location taken from surface catalogue, specifically, the event location along the fiber and perpendicular distance from the fiber. We cannot fully control the depth when locating event using one-well DAS data due to the single-component nature of DAS.

(3) In this step the data are converted to f-k domain and the workflow splits into two parallel branches. Steps (3a) and (3b), f-k filtering is used to remove downgoing (toe-ward going) and the upgoing (heel-ward going) waves, respectively.

(4) To get rid of the remaining part of direct arrival body waves' moveouts, we mute all the data below (4a) and above (4b) the line going through the apex with the slope equal to S-wave velocity (muted areas are highlighted by transparent orange triangles in Figure 2). This line needs to be slightly shifted relatively to the apex to make sure that we fully mute the direct S-waves and do not deteriorate final image. After the latter step we should see only upgoing or downgoing reflected waves.

(5) The idea of imaging in (5a) and (5b) of the workflow is that every point between the fiber at $x=0$ and the event location $[x_s,\ 0]$ acts as a potential reflection point $[x_f,\ y_f]$. With an assumption that the reflector is almost vertical and perpendicular to fiber, we compute the raytracing-based travel time of the reflected S-wave tt in a homogenous isotropic velocity model with S-wave velocity V_S:

$$tt\ = \frac{2y_f\ -\ y_r}{V_s}. \text{ [1]}$$

The "channel" y_r along the fiber where the ray of reflected wave arrives is:

$$y_r = x_s - \left(y_f - \frac{x_f\ y_f}{x_s - x_f}\right). \text{ [2]}$$

DAS data amplitude from the channel y_r at the time tt is then assigned to the tested reflection point in space. After going through all the potential reflection points between the fiber and the event location the imaging is done.

The final two steps are: (6) merging the two images of downgoing and upgoing reflected waves to form a complete image and (7) post-processing. Here, we calculate signal envelopes and apply a low-pass filter to the merged image to further enhance visibility of reflector(s). An example of the resulting image is shown at the bottom of workflow where the dark color means no reflection or data coverage, and coherent near-horizontal bright spots represent positions of near-vertical reflectors approximately perpendicular to the fiber.

Figure 2. Proposed 7-step workflow of reflector imaging using reflected S-waves recorded by DAS with an illustration of raytracing-based reflector imaging methodology.

3. RESULTS

3.1. Imaged reflectors

We demonstrate the processing results for two microseismic events (Events A and B as displayed in Figure 1) using the above-described methodology. Figure 3 shows input DAS microseismic waveforms and the resulting images of reflectors in space in two columns on the left. Each image is a 2D plane between the event location and the part of fiber from which we have DAS data.

The bright spots elongated in the direction approximately perpendicular to fiber indicate the imaged reflectors. The length of imaged reflectors is proportional to the length of reflected wave visible in the DAS data. The imaged reflectors usually do not intersect with the fiber (at the distance 0) because of the mute window around the direct arrivals (including a few wavelengths of high amplitude S-wave coda). The muting must be done to avoid distortion of the final image around apex. However, we realize that we also mute part of the reflected S-wave signal mixed with S-wave coda and thus lose information about the reflector in the vicinity of the fiber. The imaged reflectors fade out with distance from fiber similarly like the signal of reflected wave in DAS data, probably due to attenuation and larger channel offset. It does not mean that the reflectors are not longer, as we image only its visible parts illuminated by the individual microseismic event. The black color at the far distance from the fiber means no data coverage, i.e., there are no points reflecting energy back to the part of fiber we have data from. Whereas the black spaces in a narrow zone around the apex line result from muting the direct S-wave in the input data (steps (4a) and (4b) of the workflow). All the other spaces with dark colors are representing media without reflectors.

The image of Event A shows one very clear horizontal bright spot representing a reflector within 50 m from the fiber. In the DAS data, the position of imaged reflector along the fiber is corresponding to the channel where both direct S- and reflected S-waves intersect (highlighted by green dashed-line arrow in the Figure 3). There is another reflector in the image which is weaker and shorter (visible within 20 m from the fiber) than the main reflector but still with coherent brightness in the direction from fiber. The matching reflected S-wave in the DAS data is of proportionally low signal-to-noise ratio (SNR) and its amplitude quickly attenuates away from the fiber. The remaining randomly located bright spots are too small and probably result from coherent noise in the input data. Meanwhile, Event B has one approximately 30 m long reflector visible in its image.

Figure 3. Input DAS data, reflector images and LFDAS data for two example events. The green dashed-line arrows highlight position of reflectors in the images. The yellow stars represent location and origin time (only in the LFDAS data) of microseismic events.

3.2. Comparison with LFDAS and interpretation

Up to this point, we have referred to bright spots in images as reflectors because we had no clear indication of whether they can be interpreted as newly created

fractures due to hydraulic fracturing or pre-existing vertical faults in the area. To inspect whether we image one or the other we compare the images with LFDAS data. The LFDAS data are the same recorded raw DAS data as the analyzed DAS microseismic data but in a very low frequency band (< 0.1 Hz). Figure 3 shows images for both microseismic events in the middle and LFDAS data from the corresponding stage in the right column. The yellow stars placed in the LFDAS data are at the events' origin time and location along the fiber. Note that the DAS microseismic data of each event and consequently the image of reflector(s) is a snapshot of the medium around the event location at the time when event happened, whereas the LFDAS data show evolution of measured strain during the entire stage.

The LFDAS data around the origin time and location of the Event B shows a very clear signal characteristic of frac-hits. The first fracture started to open (zone of compression in blue around the extensive opening zone in red) shortly before 12 am. Later on, other fractures hit the fiber approximately 80 m aside of the first frac-hit and started to open. A few minutes later, the changes in the reservoir induced Event B recorded by DAS array. The comparison with LFDAS provides undeniable evidence that the observed S-wave is back-scattered from the newly created fracture to the monitoring fiber - position of fracture in our image aligns with the position of frac-hit in the LFDAS data (see the green dashed-line arrow). The explanation why we identified only one fracture in the image while the LFDAS shows three existing fractures at the event origin time is unclear. It is less likely to be resolution issue as the thickness of imaged fracture is smaller than the entire fractured zone. The first opened fracture (at the top in the LFDAS) is most likely not imaged due to its narrower width or because the fracture was already closed and did not create enough seismic impedance. The third fracture (at the bottom in the LFDAS) lies in the muted zone of our image (too close to the apex of microseismic event).

The LFDAS data for the stage of hydraulic fracturing when the Event A occurred is of low quality, not allowing detection of frac-hits. The source of abnormally high low-frequency noise was an injection operation taking place in the monitoring well. This caused large temporal change of temperature conditions short time before the LFDAS data was acquired. Note that the low frequency noise does not affect the DAS microseismic data while we look at much higher frequencies where the sensitivity to temperature is negligible. As the image of Event B has been proven to be showing induced fracture(s), we may expect that the similarly looking reflectors in the image of Event A are also fracture. However, we cannot prove it by comparison with frac-hit due to the noisy LFDAS.

4. DISCUSSION

4.1. Methodology

Our methodology relies on recorded signal reflected from fractures. We have used reflected S-waves, but analogically reflected P-waves might be used. Visibility of reflected waves in data depends on sensitivity of DAS monitoring sys-

tem, magnitude of microseismic event and relative geometry between source, fiber and fracture. If the microseismic event is located too close to the induced fracture (relative to distance of the event from the fiber), most of the energy is reflected to far offset channels (far from apex line in the DAS data) and the signal of the reflected wave arrives shortly after direct body wave and has almost the same moveout. Therefore, in our workflow, the reflected wave may be filtered out or muted together with the body wave signal and information about fracture is lost. Remaining energy reflected from the fracture appears close to the apex where it is usually mixing with high SNR body-wave coda which we also mute. This means that fracture imaging using reflected waves is hardly possible when the event-fracture-fiber geometry does not lead to a reflected signal clearly distinguishable from signal of direct body waves.

Our fracture imaging methodology is based on several assumptions. The raytracing is done only for reflections from a vertical fracture oriented approximately perpendicular to fiber in a homogenous isotropic velocity model. These assumptions appear to be valid in that the fractures are near vertical, and the events and monitor well are in the same horizontal formation which can be described by a single velocity structure. Similar conditions might be found in many other fields but, in general, to be able image fractures with arbitrary orientation in a complex velocity model, we would need to use more sophisticated raytracing or advanced imaging methods such as Kirchhoff migration or reverse time migration (e.g., Li et al., 2020). However, that would require more accurate event locations and stacking of many microseismic events (sources) to get a reasonable image.

One of our first steps in the workflow is manual picking and event (re-)location as we wanted to improve the initial event locations obtained from surface microseismic catalog. Without the known initial location, we would also locate the event but have only information about the event position along the fiber and distance from the fiber when located from one fiber only. The event location would have uncertainty a 360° around the axis of the horizontal well because of the axial sensitivity of DAS. Therefore, we would not know the correct orientation of imaged fractures. Note that the image is always in the plane between the event and the fiber. Of course, P- and S-wave arrivals needed for location do not have to be picked manually if an efficient auto-picking algorithm is employed.

4.2. Application

The most obvious application of the fracture imaging is processing of continuous cross-well DAS microseismic data acquired during hydraulic fracturing to map created fractures around stimulated wells. Such detailed map can have big impact on precision of DFN and its reliability. With fracture imaging we may potentially map dynamic evolution of the fracture if several microseismic events are induced and detected during the same stage around the fracture. The microseismic events provide snapshots of the surrounding reservoir at their origin times. If we are able to image fractures, it means that the fracture is already open and wide enough to reflect energy from microseismic event. With several

microseismic events following each other in time, we may see fracture growth, i.e., dynamic changes of the reflected wave visible in DAS data, and thus the lateral extent of the imaged fractures. When the fracture starts closing, seismic impedance decreases, and fracture disappears from image. Fracture closing was shown in LFDAS data by Jin & Roy (2017) as well as in time-lapse DAS VSP. Compared to the 4D inter-stage DAS VSP (Binder et al., 2020; Titov et al., 2021), our fracture imaging provides a better resolution due to higher frequency content (microseismic event as a source is closer to the fiber than surface source used for VSP) and can image fractures in 3D if the event location is known.

LFDAS monitoring has been used to monitor frac-hits. Unfortunately, as shown on example in Figure 3, LFDAS can be contaminated by noise due to temperature effects induced by injection operations in the monitor well. In such cases, fracture imaging of DAS microseismic data may provide complementary information to results from LFDAS. Furthermore, the LFDAS can detect frac-hits or strain changes only in the close vicinity of the monitoring fiber. Our fracture imaging is also able to map these frac-hits and, moreover, it has a capability to map fractures which do not intersect monitoring fiber well as the imaging space locates between the event and the monitoring fiber. From such images we can estimate fracture geometry of fractures with half-length shorter than well spacing. Of course, the disadvantage is that fracture imaging is dependent on induced microseismic events whereas LFDAS not.

5. CONCLUSIONS

We have shown examples of microseismic events recorded by DAS fiber in a horizontal well during hydraulic fracturing of unconventional reservoir. Besides direct P- and S-waves, the events have clearly visible signals of S-waves reflected at hydraulic fractures. We developed a new processing workflow to image the fracture using the reflected waves and demonstrated the conversion of DAS-based microseismic data in time to fracture image in space. Resulting images were compared to frac-hit signal in corresponding LFDAS data, supporting that the imaged reflectors are newly created hydraulic fractures. The fracture imaging can be further developed with a potential to be used for a real-time 3-D hydraulic fracture mapping when DAS monitoring is employed and induced microseismic events detected in abundance.

ACKNOWLEDGEMENTS

This work was conducted with the support of the Reservoir Characterization Project (Phase XVIII.) at the Colorado School of Mines. The authors are thankful to Bonanza Creek Energy, Inc. for support, providing the data and permission to publish the results. Authors thank Alicia Downard for helping with orientation in the data and providing coherence maps, and Xiaoyu (Rosie) Zhu for helping with the LFDAS data.

Data availability statement

The DAS microseismic data of events A and B used as examples for fracture

imaging in this study are available.

REFERENCES

Baird, A., Stork, A., Horne, S., Naldrett, G., Kendall, M., Wookey, J., Clarke, A., & Verdon, J. (2019). *Modelling of fibre-optic DAS response to microseismic arrivals in anisotropic media.* Paper presented at 81st Annual International Conference and Exhibition, EAGE, Extended Abstracts, WeR0908. https://doi.org/10.3997/2214-4609.201901244

Baldwin, C.S. (2015) Applications for fiber optic sensing in the upstream oil and gas industry. Proc. SPIE 9480, Fiber Optic Sensors and Applications XII, 94800D. https://doi.org/10.1117/12.2176226

Binder, G., Titov, A., Liu, Y., Simmons, J., Tura, A., Byerley, G., & Monk, D. (2020). Modeling the seismic response of individual hydraulic fracturing stages observed in a time-lapse DAS VSP survey. *Geophysics*, **85**, T225–T235. https://doi.org/10.1190/geo2019-0819.1

Carannante, S., D'Alema, E., Augliera, P., & Francheschin, G. (2020). Improvement of microseismic monitoring at the gas storage concession "Minerbio Stoccaggio" (Bologna, Northern Italy). *Journal of Seismology*, **24**, 967–977. https://doi.org/10.1007/s10950-019-09879-2

Cole, S., Karrenbach, M., Kahn, D., Rich, J., Silver, K., & Langton, D. (2018). *Source parameter estimation from DAS microseismic data.* Paper presented at 88$^{\text{th}}$ Annual International Meeting, SEG, Expanded Abstracts 2018, 4928-4932. https://doi.org/10.1190/segam2018-2995716.1

Grechka, V., & Heigl, W. M. (2017). *Microseismic monitoring.* Society of Exploration Geophysicists. https://doi.org/10.1190/1.9781560803485

Grechka, V., Li, Z., Howell, B., Garcia, H., & Wooltorton, T. (2017). High-resolution microseismic imaging. *The Leading Edge*, 36, 822–828. https://doi.org/10.1190/tle36100822.1

Hartog, A. H. (2017). An introduction to distributed optical fibre sensors. CRC Press.

Jin, G., & Roy, B. (2017). Hydraulic-fracture geometry characterization using low-frequency DAS signal. *The Leading Edge*, **36**, 975–980. https://doi.org/10.1190/tle36120975.1

Jin, G., Ugueto, G., Wojtaszek, M., Guzik, A., Jurick, D., & Kishida, K. (2021). Novel near-wellbore fracture diagnosis for unconventional wells using high-resolution distributed strain sensing during production. *SPE journal*, 1-10. https://doi.org/10.2118/205394-PA

Li, L., Tan, J., Schwarz, B., Staněk, F., Poiata, N., Shi, P., et al. (2020). Recent advances and challenges of waveform-based seismic location methods at multiple scales. *Reviews of Geophysics*, 58, e2019RG000667. https://doi.org/10.1029/2019RG000667

Lin, Y., & Zhang, H. (2016). Imaging hydraulic fractures by microseismic migration for downhole monitoring system. *Physics of the Earth and Planetary Interiors*, 261, 88-97. https://doi.org/10.1016/j.pepi.2016.06.010

Lim Chen Ning, I., & Sava, P. (2018). High-resolution multi-component distributed acoustic sensing. *Geophysical Prospecting*, **66**, 1111-1122. https://doi.org/10.1111/1365-2478.12634

Kwiatek, G., Bulut, F., Bohnhoff, M., & Dresen, G. (2014). High-resolution analysis of seismicity induced at Berlín geothermal field, El Salvador. *Geothermics*, **52**, 98-111. https://doi.org/10.1016/j.geothermics.2013.09.008

Lellouch, A., & Biondi, B. L. (2021). Seismic Applications of Downhole DAS. *Sensors*, **21**, 2897. https://doi.org/10.3390/s21092897

Luo, B., Lellouch, A., Jin, G., Biondi, B., & Simmons, J. (2021) Seismic inversion of shale reservoir properties using microseismic-induced guided waves recorded by distributed acoustic sensing. *Geophysics*, **86**, R383-R397. https://doi.org/10.1190/geo2020-0607.1

Luo, B., Jin, G., & Stanek, F. (2021). Near-field strain in distributed acoustic sensing-based microseismic observation. *Geophysics*, **86**, P49-P60. https://doi.org/10.1190/geo2021-0031.1

Mendecki, A. J., Lynch, R. A., & Malovichko, D. A. (2010). *Routine microseismic monitoring in mines*. Paper presented at Australian Earthquake Engineering Society Conference.

Reshetnikov, A., Kummerow, J., Buske, S., & Shapiro, S. A. (2010). *Microseismic imaging from a single geophone: KTB*. Paper presented at 80th Annual International Meeting, SEG, Expanded Abstracts, 2070–2074. https://doi.org/10.1190/1.3513252

Schultz, W.H. (2019). Time-lapse multicomponent geophone and DAS VSP processing and analysis, (Master's thesis). Colorado School of Mines, dept. of Geophysics.

Stanek, F., & Eisner, L. (2017). Seismicity induced by hydraulic fracturing in shales: A bedding plane slip model. *Journal of Geophysical Research: Solid Earth*, **122**, 10, 7912–7926. https://doi.org/10.1002/2017JB014213

Stanek, F., & Jin, G. (2021). *Reservoir characterization using DAS microseismic events*. Paper presented at First International Meeting for Applied Geoscience & Energy, Expanded Abstracts, 463-467. https://doi.org/10.1190/segam2021-3583216.1

Titov, A., Binder, G., Liu, Y., Jin, G., Simmons, J., Tura, A., Monk, D., Byerley, G., & Yates, M. (2021). Modeling and interpretation of scattered waves in interstage distributed acoustic sensing vertical seismic profiling survey. *Geophysics*, **86** (2), D93–D102. https://doi.org/10.1190/geo2020-0293.1

Verdon, J. P., Horne, S. A., Clarke, A., Stork, A. L., Baird, A. F., & Kendall, J.-M. (2020). Microseismic monitoring using a fiber-optic distributed acoustic sensor array. *Geophysics*, **85**, KS89-KS99. https://doi.org/10.1190/geo2019-0752.1

Williams-Stroud, S., Ozgen, C., & Billingsley, R. L. (2013). Microseismicity-constrained discrete fracture network models for stimulated reservoir simulation. *Geophysics*, **78**, B37–B47. https://doi.org/10.1190/geo2011-0061.1

Williams-Stroud, S., Bauer, R., Leetaru, H., Oye, V., Stanek, F., Greenberg, S., & Langet, N. (2020). Analysis of microseismicity and reactivated fault size to assess the potential for felt Events by CO2 njection in the Illinois basin. *Bulletin of the Seismological Society of America*, **110**, 2188–2204. https://doi.org/10.1785/0120200112

Zeynal, A.R., Snelling, P., Neuhaus, C.W., & Mueller, M. (2014). *Correlation of stimulated rock volume from microseismic pointsets to production data - A Horn River case study.* Paper presented at Western North American and Rocky Mountain Joint Meeting, SPE. https://doi.org/10.2118/169541-MS

Zhu, X. & Jin, G. (2021). *Analysis of cross-well fracture hits in DJ Basin, Colorado using low-frequency DAS data.* Paper presented at First International Meeting for Applied Geoscience & Energy, Expanded Abstracts, 457-462. https://doi.org/10.1190/segam2021-3582658.1

Zoback, M. D. (2012). Managing the seismic risk posed by wastewater disposal. *Earth Mag.*, 57, 38–43.

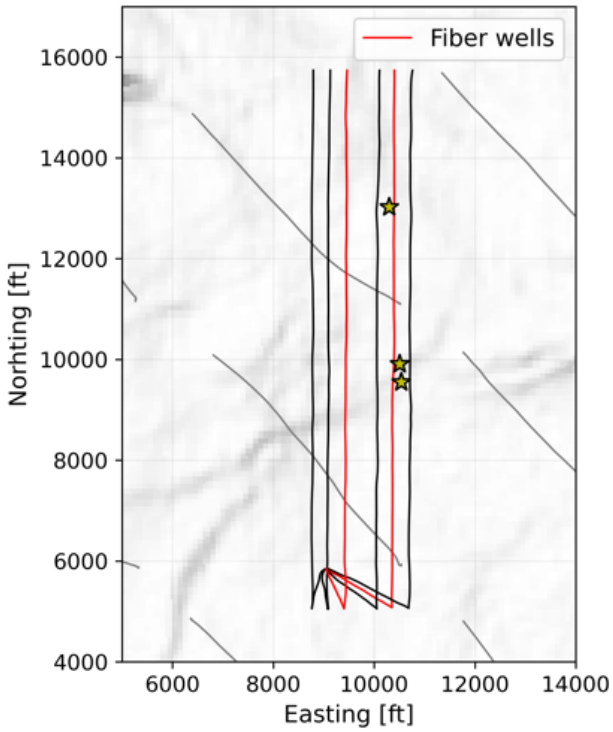

Figure 1: Upper left: A map of the horizontal wells (running N-S) and their relative positions. Wells with permanently installed fiber are shown in red. The diagonal NW-SE wells shown in gray are previously drilled production wells in the Niobrara. The yellow stars represent examples of strong microseismic events (A, B, C). The seismic coherency map in the background may indicate potential faults in the Niobrara formation. Upper right and bottom: Examples of three representative microseismic events with direct P-waves (P_D), direct S-waves (S_D), converted S- to P-waves (SP) and reflected S-waves (S_R) recorded by DAS array. The events A and B are accompanied by another weaker event with very similar moveout indicating similar location but slightly different origin time. Event C shows more complicated reflections after the direct S-wave.

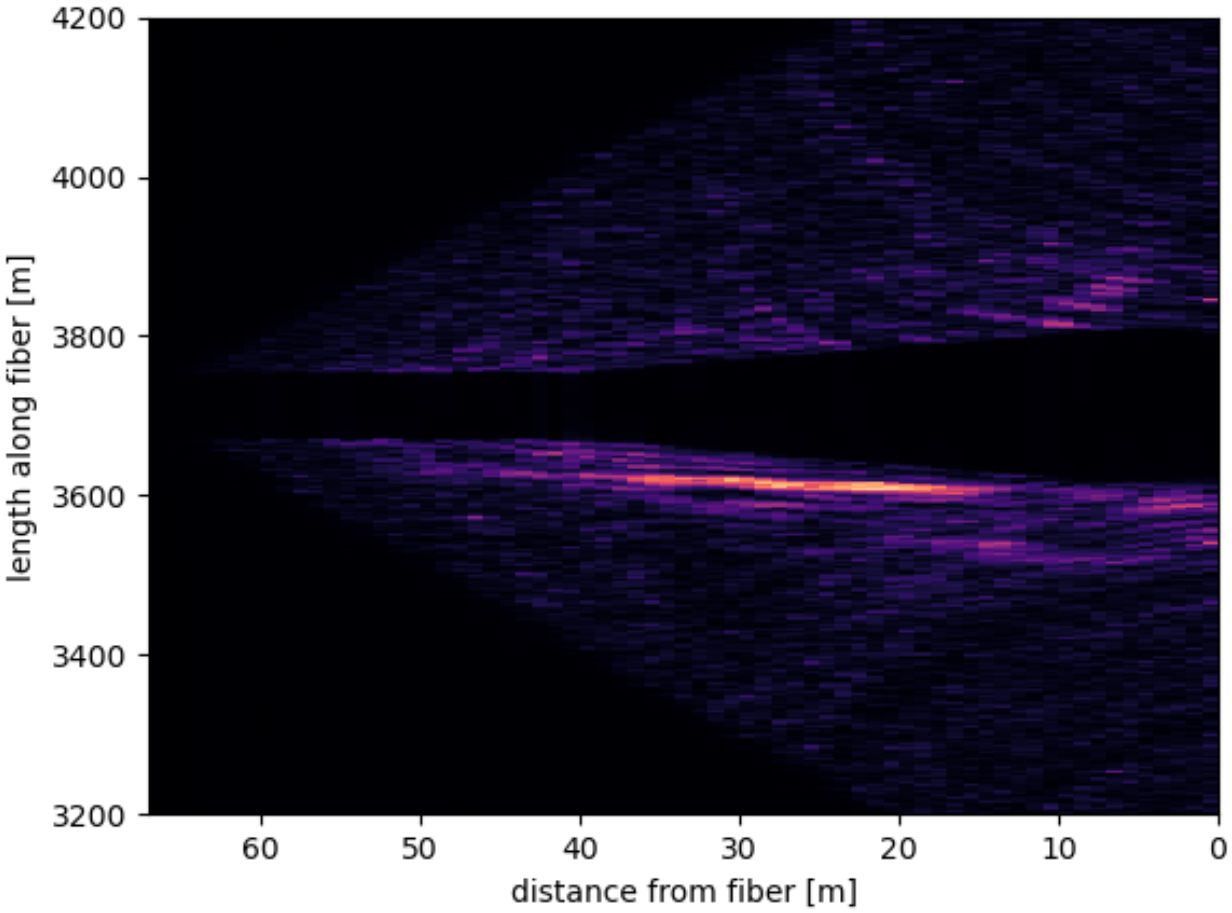

Figure 2. Proposed 7-step workflow of reflector imaging using reflected S-waves recorded by DAS with an illustration of raytracing-based reflector imaging methodology.

Figure 3. Input DAS data, reflector images and LFDAS data for two example events. The green dashed-line arrows highlight position of reflectors in the images. The yellow stars represent location and origin time (only in the LFDAS

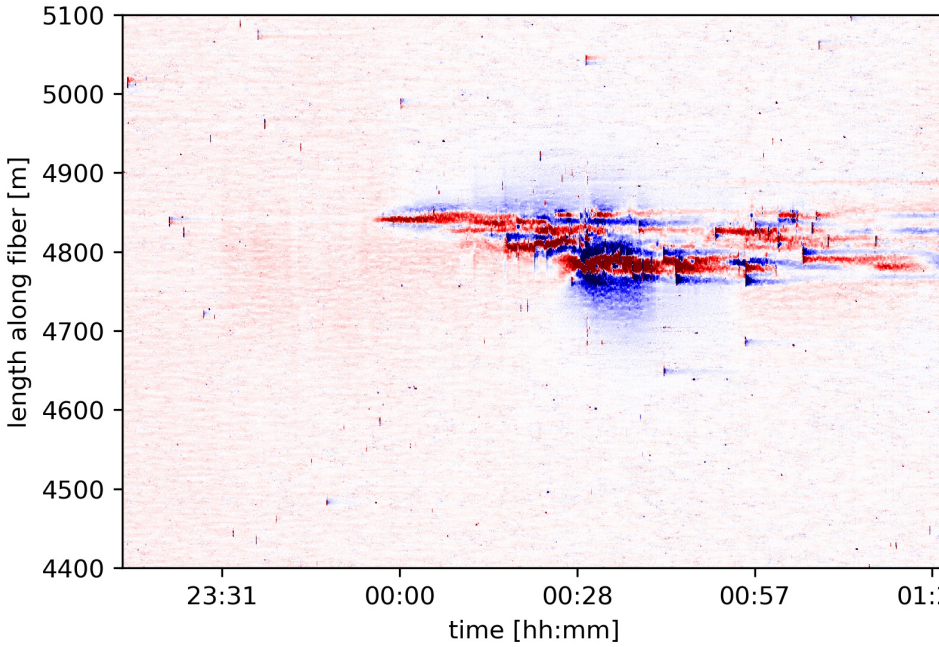

data) of microseismic events.